Effects of the absence of friction in coarse-grained molecular dynamics simulations of clay

Sara Bandera, Ph.D[1]*, Tokio Morimoto, Ph.D[2], Catherine O'Sullivan, Ph.D, M.ASCE[3], Paul Tangney, Ph.D[4] and Stefano Angioletti-Uberti, Ph.D[5]

[1]Research Fellow, Department of Civil Engineering and Architecture, University of Pavia, Pavia, Italy; *Corresponding author, email address: sara.bandera@unipv.it

[2]Assistant Professor, Department of Civil Engineering, The University of Tokyo, Tokyo, Japan

[3]Professor of Particulate Soil Mechanics, Department of Civil and Environmental Engineering, Imperial College London, United Kingdom

[4]Senior Lecturer, Department of Physics and Department of Materials, Imperial College London, United Kingdom

[5]Senior Lecturer, Department of Materials, Imperial College London, UK

Abstract

Coarse-grained molecular dynamics (CGMD) simulations can advance understanding of clay behaviour. In CGMD simulations the interactions between clay platelets are modelled and the data generated can be used to quantitatively link clay fabric to the overall material behaviour and examine its sensitivity to changes in the pore-fluid chemistry. A key element of a CGMD model is the potential function employed for particle interactions. One approach is to use Derjaguin-Landau-Verwey-Overbeek (DLVO) theory to calibrate the contact models; however, DLVO theory does not account for a frictional component in the interaction. This contribution shows that omitting a frictional force results in an unexpected overall system response. The conclusion is developed by considering CGMD data generated during one-dimensional compression tests of assemblies of 10,000 kaolinite particles modelled as flat ellipsoids. When the Gay-Berne potential function, calibrated against DLVO predictions, is used to simulate the interactions and inter-particle friction is not explicitly modelled, the resulting coefficient of earth pressure at rest $K_0 = {\sigma_h'}/{\sigma_v'}$ is equal to 1. Furthermore, the packing density obtained in the CGMD is lower than that observed experimentally. Additional data generated using DEM simulations on assemblies of spherical particles demonstrate the sensitivity of K_0 and packing density to the interparticle friction coefficient. Data presented here clearly support the need to explicitly consider a frictional-type component in particle interactions when simulating systems of clay platelets.

Keywords: Clays; Particle-scale behaviour; Friction

Introduction

The engineering properties and rheological behaviour of clays are of great importance in geotechnical engineering. Particle-scale modelling techniques have recently been used to obtain insights into the response of clay minerals to external loads (e.g. Aminpour and Sjoblom, 2019; Bandera et al., 2021; de Bono and McDowell, 2023, 2022a, 2022b; Ebrahimi et al., 2014; Pagano et al., 2020; Sjoblom, 2016; Yao and Anandarajah, 2003). The interactions between clay particles are more complex than those between sand grains. The non-contact electrostatic and van der Waals forces are sufficiently large relative to the particle inertia that they control the particle interactions and hence the overall material behaviour. In particle-scale models of sand, which mainly use the discrete element method (DEM), the inter-particle coefficient of friction, μ, is a key input parameter. However, in clay, where the non-contact interactions dominate, the relevance of explicitly accounting for friction in the contact model employed is not immediately or intuitively apparent. This contribution demonstrates that a particle-based model of clay, in which the particle units are clay platelets, and which does not include inter-particle frictional forces, predicts a non-physical response under stress controlled one-dimensional compression. Here we show that the model predicts a coefficient of lateral earth pressure of $K_0 = 1.0$. DEM simulations of assemblies of spherical particles are used here to support the argument in favour of including friction in this type of model.

Background

In soil mechanics research, particle-scale models of clay have been developed using both the discrete element method (DEM) and molecular dynamics (MD). The DEM algorithm as proposed by Cundall and Strack (1979) is now well established as a tool in geomechanics research. MD is a numerical modelling technique that is algorithmically very similar to DEM as detailed, for example, in Allen and Tildesley (2017) and Frenkel and Smit (2002). A key difference is that in MD the interactions are modelled using potential functions which describe the variation of the potential energy with separation distance, rather than the force-displacement models that are typically used in DEM. Arguably this difference is semantic as the force can be easily obtained as the derivative of the energy-separation relationship (e.g. Pagano et al., 2023). The use of MD to simulate the mechanical behaviour of assemblies of clay particles has been documented in Aminpour and Sjoblom (2019), Bandera et al. (2021), Ebrahimi et al. (2014), and Sjoblom (2016). In these contributions clay platelets are modelled either as three-dimensional ellipsoids interacting via the Gay-Berne (GB) potential (Gay and Berne, 1981) as in Ebrahimi et al. (2014) and Bandera et al. (2021), or as assemblies of spheres whose interactions are modelled using the Lennard-Jones potential (Lennard-Jones, 1931) as in Sjoblom (2016) and Aminpour and

Sjoblom (2019). These MD models are termed “coarse-grained”, and denoted as CGMD, because the particles represent assemblies of molecules (in lieu of molecules or even atoms that might be considered in classical MD) and the potential functions describe the effective interactions between the particles rather than between the constitutent molecules.

The GB potential, developed for ellipsoids, is a generalization of the Lennard-Jones potential. In both of these potentials the interaction energy is described in terms of the centre-to-centre distances between particles; the Gay-Berne potential also considers the particle orientation. However, neither potential function explicitly accounts for friction or a tangential interaction. Similarly, DLVO theory (Derjaguin and Landau, 1941; Verwey and Overbeek, 1948), which was developed to describe the behaviour of colloidal systems and is now generally accepted in soil mechanics to describe the mechanical behaviour of clay, does not consider the contribution of any frictional component, as it only accounts for the van der Waals and electrostatic interactions. Previous MD studies on clay systems have not explicitly considered friction in their simulation. This can be seen in Table 1, which presents a summary of the contact models used in MD particle-scale simulations of clay. Tangential contact models employed and friction coefficient used in DEM clay studies are also included for completeness.

Atomistic MD simulations have been used in fundamental studies of friction. For example Ringlein and Robbins (2004) investigated how the static friction develops from the potential energy of the atomic interactions using two-dimensional atomistic MD simulations by considering two walls of atoms interacting through a LJ potential. Rather than explicitly specifying a coefficient of friction, a frictional response emerged from these simulations. Ringlein and Robbins (2004) attributed static friction at the macroscopic scale to large rearrangements of atoms which force them into their energy minima and discussed various surface rearrangements to explain the available experimental evidence. They concluded that static friction depends on the surface geometry, the contact area, and on the rearrangement undergone by surface atoms; Göncü et al. (2009) indicated that sliding and rotation of particles play a role. Gao et al. (2004) documented 3D MD simulations that considered both solid surfaces and an inter surface lubricant; also in this research work the inter-molecule potentials they considered (documented in Gao et al. (1997)) do not include a friction parameter. Again, a frictional response emerged from these simulations and the data generated were used to conclude the validity of Amontons’ law (Amontons, 1699). Notably, none of these simulations consider coarse-grained particles but the molecular, atomistic nature of the system is explicitly described.

Experimental data to inform understanding of friction between clay platelets are lacking. It is challenging to accurately measure μ between two soil grains, which are characterised by small sizes. Contributions such as those by Mitchell and Soga (2005) highlighted the difficulty in defining the origin of friction between particles in fine-grained soils (i.e. clays), where inter-particle contacts are absent. Studies such as Gupta et al. (2011), Kumar et al. (2017) and Yesufu-Rufai et al. (2020) have demonstrated the potential to use AFM (atomic force microscopy) to study clay particle interactions, but we know of no AFM or SFA (surface force apparatus) data that can inform understanding of friction between clay particles.

If friction is included in a DEM or MD model, the structure of the code used in the simulations becomes more complex as the tangential force has to be calculated by summing the tangential components of the incremental relative displacements in each time-increment following contact formation (e.g. Hanley et al., 2018; Keishing et al., 2020; O'Sullivan and Bray, 2004). This need for summation requires the history of the interaction to be stored, increasing the computational (memory) requirements to run a simulation and requiring modification of data structures. An important question is thus whether or not this frictional force is important for the correct macroscopic behaviour of the system to emerge. Intuitively, friction is a non-equilibium phenomenon and one can expect other non equilibrium quantities to be affected. However, it is not clear whether other mechanical equilibrium quantities will also be affected.

Methodology and Results

Coarse-grained molecular dynamics (CGMD) simulations

The CGMD simulations discussed in this study followed the approach outlined in detail in Bandera et al. (2021). For completeness, key features are summarised here. Two virtual samples, *Mono_1* and *Poly_1*, were considered. *Mono_1* contains monodisperse ellipsoidal particles with an aspect ratio AR=10 and a major axis length (diameter) of 2 μm. *Poly_1* contains a 1:1:1 (approximate) mixture of three particle types. The average diameter is the mean value in the range suggested by Santamarina et al. (2001); the two additional diameter values were taken as 20% above and 20 % below the average. *Poly_1* contains particles with different dimensions but all having AR=10. As outlined in Bandera et al. (2021), the Gay-Berne model parameters were determined by calibration against the interaction energies predicted by the DLVO theory. Here we consider kaolinite saturated with a pore fluid having a pH=8 and a 1mM KCl concentration. In this scenario, only the long-range interactions were considered necessary for the calibration and a trial-and-error approach was used to select the parameters considering only the repulsive term of the Gay-Berne potential (Bandera et al., 2022, 2021):

$$U_{GB,Repulsive}^{sb} = 4\epsilon\left[\left(\frac{\sigma}{h_{12}+\gamma_{sb}\sigma}\right)^{12}\right]\times\eta\times\chi \qquad \text{Eq. 1}$$

where $\epsilon\ [J]$ is the energy scale, $\sigma\ [nm]$ is the length scale, $\gamma_{sb}[-]$ is a pair-wise dimensionless parameter used to shift the potential minimum and accounts for the particles' finite radii, and $h_{12}\ [nm]$ is defined as the closest distance between the surfaces of two ellipsoidal particles. The dimensionless quantities η and χ are the shape and energy anisotropies, respectively; they depend on the particle dimensions, on their relative orientation, and on the relative well-depth values, ε_a, ε_c, which are defined for face-face and edge-edge interactions for these monodisperse particles (for completeness, the equations employed to compute η and χ are given in Appendix A and described in more detail in Bandera (2022)). The DLVO prediction of the variation in potential energy with particle separation was obtained considering clay surface potential data from Gupta et al. (2011) and was visually compared with the GB prediction to select the optimal parameters listed in Table 2 and Table 3 for *Mono_1* and *Poly_1*, respectively. The potential function detailed in Eq. 1 was implemented in a modified version of the open-source MD code LAMMPS (Bandera et al., 2022; Thompson et al., 2022). The systems of clay particles were assumed to be fully saturated and fully drained and the influence of pore water chemistry on interactions is accounted for via the potential function. Samples containing 10,000 kaolinite particles were created by placing randomly oriented ellipsoids on a simple cubic lattice; the centre-to-centre spacing between ellipsoids was larger than the particle diameter to avoid overlap. Periodic boundary conditions were used in all three directions. The initial generated sample had a cuboidal geometry with an aspect ratio of 4, so that $L_x = L_y = {}^{L_z}/_{4}$ (Figure 1(a) shows *Mono*_1 at this point). Figure 1(b) shows the final specimen geometry (again for *Mono_1*); the particle arrangement is comparable with published SEM images for one-dimensionally compressed kaolinite samples saturated at high pH values (e.g. Pedrotti and Tarantino, 2018).

Immediately after generation the specimens were almost gaseous, meaning that they had very low density, a very high void ratio ($e \approx 19.5$) and there was little interaction amongst particles. The horizontal dimensions (x and y directions) of the simulation boxes remained fixed during the simulation. Quasi-static one-dimensional compression was simulated by linearly increasing the external pressure in the vertical (z) direction to $100\ kPa$ in a NPT simulation where the kinetic temperature (T) and the number of particles (N) remained constant. The evolution of the sample geometry with increasing vertical pressure (i.e. vertical effective stress,σ_v') during

compression is illustrated in Figure 2 for the *Mono_1* sample. Following Bandera et al. (2021), the simulations involved a series of equilibration stages prior to performing one-dimensional compression, as shown in Figure 3. For each sample, following generation, a NVE simulation, in which particles move and interact with each other while conserving energy ($E_{MD,Tot}$) was performed. The initial configurations were artificial, and so, at the beginning of the NVE simulation, there were large forces between the particles. These resulting large accelerations and velocities meant that energy was not perfectly conserved for a for a few time-steps at the beginning (Allen and Tildesley, 1987; Tuckerman, 2010). During this NVE simulation, the temperature (T) calculated from the average of the particles' kinetic energies increased to a high value, indicating that the system that had not yet reached thermal equilibrium. The sample in the non-equilibrated stage was then subjected to a NVT simulation in which its temperature was reduced to room temperature by applying a Nose'-Hoover thermostat (Shinoda et al., 2004) and the system was left to equilibrate until the temperature had stabilised.

Both the kinetic temperature T (which is linked to the kinetic energy of the particles) and the total energy ($E_{Tot,MD}$) were monitored throughout the 1D compression as illustrated for the *Mono_1* sample in Figure 4. T oscillated around the prescribed value of 300 K (Figure 4(a)) indicating that the simulation was stable, while, as expected, the energy increased with increasing pressure (Figure 4(b)). The observed variation in e is plotted against $\log(\sigma_v')$ in Figure 5; the solid line indicates the *Mono_1* sample, while the dashed line refers to the *Poly_1* sample. At 100 kPa void ratio values for the Poly_1 sample are slightly smaller than those of the Mono_1 sample, as one would expect with increasing polydispersity (e.g. Youd (1973)). The small difference in void ratio values in comparison to what might be expected in comparing monodisperse and polydisperse packings can be attributed to the size-dependency of the potential-energy separation relationship (see data in Bandera et al. (2021)) and the very flat particle topology utilized.

The average slope of the lines in Figure 5, gives a compression index (C_c) computed as $C_c = {\Delta e}/{\log\left(\frac{\sigma_{vf}'}{\sigma_{v0}'}\right)}$.

Considering the range of stresses between $\sigma_{v0}' = 10\ kPa$ and $\sigma_{vf}' = 100\ kPa$ $C_c \approx 0.24$ for Mono_1 and $C_c \approx 0.26$ for Poly_1. These values are in reasonable agreement with the experimental data in Pedrotti and Tarantino (2018). In their experiments, Pedrotti and Tarantino considered kaolinite saturated with alkaline pore water with pH=9; their data give a $C_c \approx 0.25$ (computed from their published data over the same stress range considered here). The packing density of the virtual specimens, both at the beginning and at the end of 1D compression, is lower compared to that observed in experiments. Pedrotti and Tarantino reported void ratios of ~ 1.36 and ~ 1.14 at $10\ kPa$ and $100\ kPa$ respectively. The void ratios are lower than those observed in Pedrotti and

Tarantino's experiments. This may partly be due to differences in specimen generation, which are inevitable. However, the absence of friction likely contributes to the discrepancy. The data on Figure 9 clearly show that the void ratio increases as the coefficient of friction increases in the case of spherical particles. Furthermore de Bono and McDowell (2023) showed the dependency of inter-particle friction μ on the void ratio e of virtual kaolinite specimens generated using DEM.

Figure 6 displays the rose diagrams of the initial and final particle orientations for *Mono_1*. As expected, the particle orientations are clearly aligned so that their minor semi-axis is in the direction of the deformation following one-dimensional compression; this is again in line with experimental observations of particle alignment in 1D compression tests using scanning electron microscopy (SEM) images (e.g. Pedrotti and Tarantino, 2018; Wang and Siu, 2006). The results presented in Figure 1 to Figure 6 indicate the model can describe reasonably well the behaviour of a kaolinite element tests subjected to 1D compression. However, when the (effective) stress tensor was computed, the following result was obtained:

$$\begin{bmatrix} \sigma'_{xx} & \sigma'_{xy} & \sigma'_{xz} \\ \sigma'_{yx} & \sigma'_{yy} & \sigma'_{yz} \\ \sigma'_{zx} & \sigma'_{zy} & \sigma'_{zz} \end{bmatrix} = \begin{bmatrix} 103{,}92 & 0.02 & -0.13 \\ 0.02 & 104.4 & 0.07 \\ -0.08 & 0.04 & 101{,}73 \end{bmatrix} kPa \qquad \text{Eq. 2}$$

These stress data emerged as an output from LAMMPS (which included both the virial and kinetic components) and were also confirmed in post processing that included an integration (summation) over each interaction such that $\sigma'_{ij} = \frac{1}{N}\sum_{c=1}^{N} f_i^c l_j^c$ where N is the total number of interactions, f_i^c is the force vector for interaction c, and l_j^c is the branch vector connecting the centroids of the two ellipsoids that define interaction c (see Bandera (2022)). The tensor in Eq. 2 clearly indicates that an almost isotropic stress state was obtained in the sample, in contrast to our expectations on soil behaviour. For example, Atkinson et al. (1987) give a value of $K_0 = 0.66$ for normally consolidated kaolin. In fact, the stress indicated in Eq. 2 is very close to that which we would expect in a fluid where the pressure is the same in all directions irrespective of the orientation of the applied stress.

Several studies performed in physics and material science have focussed on the behaviour of frictionless granular systems (i.e. Azéma et al., 2018; Ouaguenouni and Roux, 1997; Peyneau and Roux, 2008). Disordered assemblies of frictionless particles, i.e. without an ordered crystalline structures, can be seen as amorphous materials like suspensions or colloidal glasses (Azéma et al., 2018).

Figure 7 (a), (b) and (c) show 2D projections of the contacts on the $x - y$ (a), $x - z$ (b) and $y - z$ (c) planes in the clay sample subjected to 1D compression at a stress level of $100\ kPa$. Segments indicate the direction of the contacts, and their thickness is proportional to the force that develops. Figure 7 (d), (e) and (f) include rose diagrams showing the contact orientation at the end of the 1D compression. These rose diagrams are colour-coded according to the magnitude of the force. As can be seen, and as it was expected, the force distribution is isotropic in the $x - y$ plane, which is orthogonal to the load direction. On the other hand, Figure 7 (e) and (f) show that, while higher forces develop in the loading direction (i.e. vertical), a larger number of weaker contacts develop in the horizontal direction causing the isotropy of the stress tensor observed. In other words, since the box dimensions cannot change along the x and y directions, the particles rearrange themselves to increase the resulting stress in these directions. Similar results were also obtained for the *Poly_1* sample and are summarised in Bandera (2022).

Discrete Element Method (DEM) simulations of spherical particles

Implementation of a GB-type potential that includes a frictional component is non-trivial because of the need to store the history of the interaction and this was beyond the scope of the current research. Therefore, to explore the hypothesis that a frictional component is needed to improve the model's performance, we performed a series of DEM simulations of one-dimensional compression using samples containing approximately 5,000 spheres with a coefficient of uniformity C_u = 1.2, and a mean particle diameter D_{50} = 1.2 mm as shown in Figure 8. These simulations used a modified version of the Granular LAMMPS package; Huang (2014) and Otsubo (2016) documented validation of this code including its ability to capture the stress-dependent or frictional response of granular soils.

As was the case in the CGMD simulations using the GB potential, periodic boundary conditions were employed in all three directions. A simplified Hertz-Mindlin contact model with a particle shear modulus $G = 29\ GPa$ and a particle Poisson's ratio of $\nu = 0.2$ was employed. The DEM samples were prepared considering different friction coefficients ranging from $\mu = 1 \times 10^{-3}$ to $\mu = 0.34$ and were subjected to an isotropic compression to $1\ kPa$, followed by a quasi-static one-dimensional compression to $\sigma'_v = 100\ kPa$. The initial sample aspect ratio was 1 and the final sample aspect ratio was close to 1. Figure 9 summarises the variation of the values of the parameter K_0 with the friction coefficient μ. As can be seen, when μ is close to 0, the value of K_0 is very close to 1, suggesting that the sample is almost isotropic. As μ increases to attain values that exceed the value of μ =0.24 reported for static friction in the experiments by Senetakis et al. (2013), who considered Leighton Buzzard sand, the value of K_0 reduces to $K_0 = 0.76$ at $\mu = 0.34$. Noting that the horizontal axis on Figure 9

uses a logarithmic scale, it is clear that K_0 is very sensitive to changes in the friction coefficient employed in the simulation over the range $\sim 0 \leq \mu \leq 0.34$. The very low void ratio of the virtual specimens considered in the CGMD simulations in comparison to physical experimental data was noted above. Figure 9 also shows a clear dependence of e_{100KPa} on the inter-particle friction. This result is again in line with the literature as it is known that the packing density of virtual specimens in DEM simulations is controlled by changing the inter-particle friction. The absence of these forces in the CGMD simulations of clay is likely one of the reasons of the differences between experimental and numerical results discussed above.

Figure 10 and Figure 11 show the force networks and contact orientations in the DEM samples generated with $\mu = 1 \times 10^{-3}$ and $\mu = 0.34$, respectively. Referring to Figure 10(a) and (b), when a very low friction value is considered, there is not a clear path for force transmission and there is a homogeneous distribution of forces in terms of both intensity and quantity. However, when $\mu = 0.34$ is used, Figure 11(a) shows a clear network for force transmission; thicker segments can be clearly seen in the vertical direction (e.g. that of the applied load). These segments carry a greater force compared to those oriented perpendicularly. Similar conclusions can also be drawn by looking at Figure 11(b), where a difference between the intensity of the forces in the x and y direction can be seen.

Conclusions

The use of particle-based modelling to simulate clay for geotechnical engineering applications is not well developed. In particular, CGMD simulations of clay are still limited, and a detailed understanding of their use is essential to study the engineering behaviour of clay. This contribution has addressed an ambiguity/inconsistency in current approaches to simulating the mechanical behaviour of clay at the particle scale; specifically, whether or not it is necessary for inter-particle frictional forces to be explicitly modelled when simulating the interactions between particles. We are not aware of any previous study on clay using CGMD which explicitly modelled the friction between particles. A tangential component in the contact model was included by Sjoblom (2016) and Aminpour and Sjoblom (2019); simulating friction would also require a tangential spring (coupled with a slider). For these simulations with a tangential force (tangential interaction), they obtained a coefficient of pressure at rest of K0~0.85 in their 1D consolidation tests.

This contribution considered CGMD simulations of one-dimensional compression of a monodisperse and a polydisperse system of 10,000 ellipsoids with a large aspect ratio interacting via a modified GB potential using CGMD. From those simulations we were able to conclude that:

a. The compression curve $e - \log(\sigma_v')$, the compression index C_c, and the rose diagram at the end of the compression phase, showing particles orientating with their minor semi-axis along the direction of compression, are in line with the expected behaviour for a sample of clay, saturated at high pH, and subjected to 1D consolidation.

b. The stress tensor computed showed an isotropic response to an anisotropic load scenario predicting a value of $K_0 \sim 1$. This result is not physical and conflicts with the known behaviour of soil. Rose diagrams of the forces developed within the specimen at the end of compression show that forces transmitting interparticle interactions in the vertical direction are fewer than those transmitting interparticle interactions in the horizontal direction but have greater magnitude.

c. DEM simulations of assemblies of spherical particles where the coefficient of friction was explicitly simulated and systematically varied showed that, as the friction coefficient μ approaches the value $\mu \rightarrow 0$ (frictionless material), $K_0 \approx 1$, just as was obtained in our CGMD simulations. As μ was systematically increased, K_0 reduced. This observation aligns with other research studies considering frictionless spheres.

d. We showed that the packing density of the virtual specimens of spheres at the end of 1D compression (e_{100kPa}) is strongly influenced by the inter-particle friction coefficient. This provides a plausible explanation for the lower void ratio observed in our CGMD clay simulations in comparison with published experimental data.

Our CGMD data, interpreted with reference to the available DEM simulation datasets, indicate that at the scale we consider in CGMD, where each simulated particle represents a clay platelet, we must explicitly consider friction to capture a physically meaningful overall response. Reference to the literature shows that in the case of MD simulations that explicitly consider atoms and molecules friction is not explicitly modelled, rather in simulations considering interfaces friction emerges from the simulation data. Further studies need to be developed to explicitly account for friction in CGMD simulations of clay, as it is already done in DEM. This is not trivial as it would have implications on the memory needed to store the information on the history of contacts. Furthermore, it is not clear at what point (i.e. at which separation distance) a frictional force should be activated when non-contacting particles are simulated. In this contribution we considered a purely repulsive potential which is an idealisation of the DLVO theory, and it may be that friction should only be activated when the separation distance is within a certain limit. A more sophisticated interaction potential capable of describing the non-monotonic nature of the dependency of

energy on separation distance as predicted by DLVO theory may be required. If this potential was implemented we might consider friction to be activated at particle separations smaller that the separation distance associated with the energy barrier, that is outlined in, for example, Israelachvili (2011).

Data Availability Statement

All data, models or code that support the findings of this study are available from the corresponding author upon reasonable request.

Acknowledgements

Dr. Bandera's research was funded by the Leverhulme Trust with Project no. RPG-2017-055. Dr. Morimoto's contribution to this manuscript was supported thanks to funding from the European Union's Horizon 2020 research and innovation programme under the Marie Skłodowska-Curie grant agreement MATHEGRAM No 813202. Simulations were carried out using the High-Performance Computer (HPC) facilities at Imperial College London.

Appendix A: Calculation of shape and energy anisotropy (η and χ)

The parameters η and χ are defined as (Everaers and Ejtehadi, 2003):

$$\eta = \left[\frac{2s_1 s_2}{\det(\boldsymbol{G_{12}})}\right]^{\frac{\upsilon}{2}} \text{ and } \chi = \left(2\hat{\boldsymbol{r}}_{\boldsymbol{12}}^{\boldsymbol{T}}\boldsymbol{B}_{\boldsymbol{12}}^{-\boldsymbol{1}}\hat{\boldsymbol{r}}_{\boldsymbol{12}}\right)^{\mu} \quad \text{Eq. A1}$$

$\boldsymbol{G_{12}}$ is computed as:

$$\boldsymbol{G_{12}} = \boldsymbol{R_1^T S_1^2 R_1} + \boldsymbol{R_2^T S_2^2 R_2} \quad \text{Eq. A2}$$

where $\boldsymbol{S_i} = diag(a_i, b_i, c_i)$ is the shape matrix for particle i. This matrix depends on the three principal radii of the particle a_i, b_i and c_i; $\boldsymbol{R}_i$ is the rotation matrix describing the orientation of the local particle frame relative to the system global frame and is derived from the quaternions describing particles orientation in MD. In our case $a_i = b_i = {}^{D}/_{2}$ and $c_i = {}^{\delta}/_{2}$, where D is the diameter of the particle and δ its thickness.

s_1 and s_2 are scalar values functions of the semi-axes lengths of the particles considered and are computed as:

$$s_i = [a_i b_i + c_i c_i][a_i b_i]^{\frac{1}{2}} \quad \text{Eq. A3}$$

The exponent for the orientation-dependent shape function η is ν. As explained by Brown et al. (2009), this parameter is empirically determined and usually a value of 1 is suggested.

$\hat{\boldsymbol{r}}_{\boldsymbol{12}}$ is the normalised distance computed as:

$$\hat{\boldsymbol{r}}_{\boldsymbol{12}} = \frac{\boldsymbol{r_{12}}}{|\boldsymbol{r_{12}}|} \quad \text{Eq. A4}$$

where $|\boldsymbol{r_{12}}|$ $[nm]$ is the norm of the centre-to-centre distance between the two particles.

$\boldsymbol{B_{12}}$ is given by the following equation:

$$\boldsymbol{B_{12}} = \boldsymbol{R_1^T E_1 R_1} + \boldsymbol{R_2^T E_2 R_2} \quad \text{Eq. A5}$$

where $\boldsymbol{E}_i = diag\left(\varepsilon_{ia}^{-1/\mu}, \varepsilon_{ib}^{-1/\mu}, \varepsilon_{ic}^{-1/\mu}\right)$ represents the energy matrix for particle i; $\varepsilon_{ia}, \varepsilon_{ib}$ and ε_{ic} are the relative well depths defined for face-to-face, side-to-side and edge-to-edge interactions, respectively, while μ is an empirically determined exponent and was taken equal to 2 in this research, as suggested by Brown et al. (2009).

Notation

$C_c[-]$	Compression index
$D_{50}\ [mm]$	Mean particle diameter
$e\ [-]$	Void ratio
e_{100kPa}	Void ratio at the end of 1D compression (i.e. $\sigma'_{v0} = 100\ kPa$)
$G\ [Pa]$	Shear modulus
$h_{12}\ [nm]$	Closest distance between particle surfaces used in repulsive GB potential function
$K_0 = \frac{\sigma'_h}{\sigma'_v}\ [-]$	Coefficient of lateral earth pressure at rest
$L_x, L_y, L_z\ [nm]$	Specimen dimensions along Cartesian axes
$U^{sb}_{GB,\text{Repulsive}}$	Repulsive component of the pair-wise Gay-Berne potential energy computed using γ_{sb}
$\gamma_{sb}[-]$	Pair-wise shift of the potential minimum used in repulsive GB potential function
$\epsilon\ [J]$	Energy scale used in repulsive GB potential function
$\varepsilon_a\ [-]$	Relative well depth value for face-face interaction
$\varepsilon_c\ [-]$	Relative well depth value for edge-edge interaction
$\eta\ [-]$	Shape anisotropy used in repulsive GB potential function
$\mu\ [-]$	Friction coefficient
$\nu\ [-]$	Poisson's ratio
$\sigma\ [nm]$	Length scale used in repulsive GB potential function
$\sigma'_h\ [kPa]$	Horizontal normal stress
$\sigma'_v\ [kPa]$	Vertical normal stress.
$\sigma_{ij}\ [kPa]$	Component of stress tensor in Cartesian coordinate system, e.g. σ_{xx}, σ_{xy}, etc.
σ'_{v0}	Initial vertical effective stress considered for the evaluation of the compression index C_c
σ'_{vf}	Final vertical effective stress considered for the evaluation of the compression index C_c
$\chi\ [-]$	Energy anisotropy used in repulsive GB potential function

References

Allen, M.P., Tildesley, D.J., 2017. Computer Simulation of Liquids. Oxford University Press. https://doi.org/10.1093/oso/9780198803195.001.0001

Allen, M.P., Tildesley, D.J., 1987. Computer Simulation of Liquids. Oxford Science Publications.

Aminpour, P., Sjoblom, K.J., 2019. Multi-scale modelling of kaolinite triaxial behaviour. Géotechnique Lett. 9, 178–185. https://doi.org/10.1680/jgele.18.00194

Amontons, G., 1699. De la Resistance Causée dans les Machines. Mém. Académie R. A 257–282.

Anandarajah, A., 2000. Numerical simulation of one-dimensional behaviour of a kaolinite. Géotechnique 50.

Atkinson, J.H., Richardson, D., Robinson, P.J., 1987. Compression and Extension of K0 Normally Consolidated Kaolin Clay. J. Geotech. Eng. 113, 1468–1482. https://doi.org/10.1061/(ASCE)0733-9410(1987)113:12(1468)

Azéma, É., Radjaï, F., Roux, J.-N., 2018. Inertial shear flow of assemblies of frictionless polygons: Rheology and microstructure. Eur. Phys. J. E 41, 2. https://doi.org/10.1140/epje/i2018-11608-9

Bandera, S., 2022. Fundamental Analysis of the Influence of Structure on Clay Behaviour (PhD Thesis). Imperial College London, London.

Bandera, S., O'Sullivan, C., Tangney, P., Angioletti-Uberti, S., 2021. Coarse-grained molecular dynamics simulations of clay compression. Comput. Geotech. 138, 104333. https://doi.org/10.1016/j.compgeo.2021.104333

Bandera, S., O'Sullivan, Catherine, Tangney, Paul, Angioletti-Uberti, Stefano, 2022. Modified LAMMPS Gay-Berne subroutine to simulate purely repulsive colloidal systems. https://doi.org/10.5281/ZENODO.7070633

Brown, W.M., Petersen, M.K., Plimpton, S.J., Grest, G.S., 2009. Liquid crystal nanodroplets in solution. J. Chem. Phys. 130. https://doi.org/10.1063/1.3058435

Cundall, P.A., Strack, O.D.L., 1979. A discrete numerical model for granular assemblies. Géotechnique 29, 47–65. https://doi.org/10.1680/geot.1979.29.1.47

de Bono, J., McDowell, G., 2023. Simulating multifaceted interactions between kaolinite platelets. Powder Technol. 413, 118062. https://doi.org/10.1016/j.powtec.2022.118062

de Bono, J.P., McDowell, G.R., 2022a. Discrete element modelling of normal compression of clay. J. Mech. Phys. Solids 162, 104847. https://doi.org/10.1016/j.jmps.2022.104847

de Bono, J.P., McDowell, G.R., 2022b. Some important aspects of modelling clay platelet interactions using DEM. Powder Technol. 398, 117056. https://doi.org/10.1016/j.powtec.2021.117056

Derjaguin, B., Landau, L., 1941. Theory of the stability of strongly charged lyophobic sols and of the adhesion of strongly charged particles in solutions of electrolytes. Acta Physicochim 14. https://doi.org/10.1016/0079-6816(93)90013-L

Ebrahimi, D., Whittle, A.J., Pellenq, R.J.-M., 2014. Mesoscale properties of clay aggregates from potential of mean force representation of interactions between nanoplatelets. J. Chem. Phys. 140, 154309. https://doi.org/10.1063/1.4870932

Everaers, R., Ejtehadi, M.R., 2003. Interaction potentials for soft and hard ellipsoids. Phys. Rev. E 67, 041710. https://doi.org/10.1103/PhysRevE.67.041710

Frenkel, D., Smit, B., 2002. Understanding molecular simulation: from algorithms to applications, 2nd ed. ed, Computational science series. Academic Press, San Diego.

Gao, J., Luedtke, W.D., Gourdon, D., Ruths, M., Israelachvili, J.N., Landman, U., 2004. Frictional Forces and Amontons' Law: From the Molecular to the Macroscopic Scale. J. Phys. Chem. B 108, 3410–3425. https://doi.org/10.1021/jp036362l

Gao, J., Luedtke, W.D., Landman, U., 1997. Structure and solvation forces in confined films: Linear and branched alkanes. J. Chem. Phys. 106, 4309–4318. https://doi.org/10.1063/1.473132

Gay, J.G., Berne, B.J., 1981. Modification of the overlap potential to mimic a linear site–site potential. J. Chem. Phys. 74, 3316–3319. https://doi.org/10.1063/1.441483

Göncü, F., Durán, O., Luding, S., Nakagawa, M., Luding, Stefan, 2009. Jamming in frictionless packings of spheres: determination of the critical volume fraction, in: AIP Conference Proceedings. Presented at the Powders and Grains 2009: Proceedings of the 6th International

Conference on Micromechanics of Granular Media, AIP, Golden (Colorado), pp. 531–534. https://doi.org/10.1063/1.3179980
Guo, Y., Yu, X., 2019. A holistic computational model for prediction of clay suspension structure. Int. J. Sediment Res. 34, 345–354. https://doi.org/10.1016/j.ijsrc.2018.12.002
Gupta, V., Hampton, M.A., Stokes, J.R., Nguyen, A.V., Miller, J.D., 2011. Particle interactions in kaolinite suspensions and corresponding aggregate structures. J. Colloid Interface Sci. 359, 95–103. https://doi.org/10.1016/j.jcis.2011.03.043
Hanley, K.J., Huang, X., O'Sullivan, C., 2018. Energy dissipation in soil samples during drained triaxial shearing. Géotechnique 68, 421–433. https://doi.org/10.1680/jgeot.16.P.317
Huang, X., 2014. Exploring critical-state behaviour using DEM (Doctoral Dissertation). The University of Hong Kong and Imperial College London.
Israelachvili, J.N., 2011. Intermolecular and surface forces, 3rd ed. ed. Academic press, Burlington (Mass.).
Jaradat, K.A., Abdelaziz, S.L., 2019. On the use of discrete element method for multi-scale assessment of clay behavior. Comput. Geotech. 112, 329–341. https://doi.org/10.1016/j.compgeo.2019.05.001
Keishing, J., Huang, X., Hanley, K.J., 2020. Energy dissipation in soil samples during cyclic triaxial simulations. Comput. Geotech. 121, 103481. https://doi.org/10.1016/j.compgeo.2020.103481
Kumar, N., Andersson, M.P., van den Ende, D., Mugele, F., Siretanu, I., 2017. Probing the Surface Charge on the Basal Planes of Kaolinite Particles with High-Resolution Atomic Force Microscopy. Langmuir 33, 14226–14237. https://doi.org/10.1021/acs.langmuir.7b03153
Lennard-Jones, J.E., 1931. Cohesion. Proc. Phys. Soc. 43, 461–482. https://doi.org/10.1088/0959-5309/43/5/301
Liu, J., Lin, C.-L., Miller, J.D., 2015. Simulation of cluster formation from kaolinite suspensions. Int. J. Miner. Process. 145, 38–47. https://doi.org/10.1016/j.minpro.2015.07.004
Mitchell, J.K., Soga, K., 2005. Fundamentals of soil behavior, 3rd ed. ed. John Wiley & Sons, Hoboken, N.J.
O'Sullivan, C., Bray, J.D., 2004. Selecting a suitable time step for discrete element simulations that use the central difference time integration scheme. Eng. Comput. 21, 278–303. https://doi.org/10.1108/02644400410519794
Otsubo, M., 2016. Particle scale analysis of soil stiffness and elastic wave propagation (PhD Thesis). Imperial College London, London.
Ouaguenouni, S., Roux, J.-N., 1997. Force distribution in frictionless granular packings at rigidity threshold. Europhys. Lett. EPL 39, 117–122. https://doi.org/10.1209/epl/i1997-00324-1
Pagano, A.G., Alonso-Marroquin, F., Ioannidou, K., Radjaï, F., O'Sullivan, C., 2023. Clay micromechanics: mapping the future of particle-scale modelling of clay, in: Proceedings of the 8th International Symposium on Deformation Characteristics of Geomaterials. Presented at the IS-Porto 2023.
Pagano, A.G., Magnanimo, V., Weinhart, T., Tarantino, A., 2020. Exploring the micromechanics of non-active clays by way of virtual DEM experiments. Géotechnique 70, 303–316. https://doi.org/10.1680/jgeot.18.P.060
Pedrotti, M., Tarantino, A., 2018. An experimental investigation into the micromechanics of non-active clays. Géotechnique 68, 666–683. https://doi.org/10.1680/jgeot.16.P.245
Peyneau, P.-E., Roux, J.-N., 2008. Frictionless bead packs have macroscopic friction, but no dilatancy. Phys. Rev. E 78, 011307. https://doi.org/10.1103/PhysRevE.78.011307
Ringlein, J., Robbins, M.O., 2004. Understanding and illustrating the atomic origins of friction. Am. J. Phys. 72, 884–891. https://doi.org/10.1119/1.1715107
Santamarina, C., J., Klein, K., A., Fam, M., A., 2001. Soils and Waves: Particulate Materials Behavior, Characterization and Process Monitoring. Wiley.
Senetakis, K., Coop, M.R., Todisco, M.C., 2013. The inter-particle coefficient of friction at the contacts of Leighton Buzzard sand quartz minerals. Soils Found. 53, 746–755. https://doi.org/10.1016/j.sandf.2013.08.012
Shinoda, W., Shiga, M., Mikami, M., 2004. Rapid estimation of elastic constants by molecular dynamics simulation under constant stress. Phys. Rev. B - Condens. Matter Mater. Phys. 69. https://doi.org/10.1103/PhysRevB.69.134103

Sjoblom, K.J., 2016. Coarse-Grained Molecular Dynamics Approach to Simulating Clay Behavior. J. Geotech. Geoenvironmental Eng. 142, 06015013. https://doi.org/10.1061/(ASCE)GT.1943-5606.0001394

Thompson, A.P., Aktulga, H.M., Berger, R., Bolintineanu, D.S., Brown, W.M., Crozier, P.S., in 't Veld, P.J., Kohlmeyer, A., Moore, S.G., Nguyen, T.D., Shan, R., Stevens, M.J., Tranchida, J., Trott, C., Plimpton, S.J., 2022. LAMMPS - a flexible simulation tool for particle-based materials modeling at the atomic, meso, and continuum scales. Comput. Phys. Commun. 271, 108171. https://doi.org/10.1016/j.cpc.2021.108171

Tuckerman, M.E., 2010. Statistical Mechanics: Theory and Molecular Simulation. Oxford University Press, 2010.

Verwey, E.J.W., Overbeek, J.T.G., 1948. Theory of the Stability of Lyophobic Colloids: The Interaction of Sol Particles Having an Electric Double Layer.

Wang, Y.-H., Siu, W.-K., 2006. Structure characteristics and mechanical properties of kaolinite soils. II. Effects of structure on mechanical properties. Can. Geotech. J. 43, 601–617. https://doi.org/10.1139/t06-027

Yao, M., 2001. Three-Dimensional Discrete Element Method Analysis of Cohesive Sols (PhD Thesis). John Hopkins University, USA.

Yao, M., Anandarajah, A., 2003. Three-Dimensional Discrete Element Method of Analysis of Clays. J. Eng. Mech. 129, 585–596. https://doi.org/10.1061/(ASCE)0733-9399(2003)129:6(585)

Yesufu-Rufai, S., Rücker, M., Berg, S., Lowe, S.F., Marcelis, F., Georgiadis, A., Luckham, P., 2020. Assessing the wetting state of minerals in complex sandstone rock in-situ by Atomic Force Microscopy (AFM). Fuel 273, 117807. https://doi.org/10.1016/j.fuel.2020.117807

Youd, T.L., 1973. Factors Controlling Maximum and Minimum Densities of Sands. ASTM Spec. Tech. Publ.

Tables and Figures

Table 1. Information on particle-scale DEM/MD studies on clay.

Reference	**Anandarajah (2000)**	**Pagano et al. (2020)**	**Yao (2001); Yao and Anandarajah (2003)**	**Jaradat and Abdelaziz (2019)**	**Guo and Yu, (2019)**	**de Bono and McDowell (2023, 2022a, 2022b)**	**Ebrahimi et al. (2014)**	**Liu et al. (2015)**	**Sjoblom (2016)**	**Aminpour and Sjoblom (2019)**
Numerical technique	DEM	DEM	DEM	DEM	DEM	DEM	MD	MD	MD	MD
2D/3D	2D	2D	3D	3D	3D	3D	3D	3D	3D	3D
Material modelled	Kaolinite	Kaolinite	Kaolinite	Kaolinite	Kaolinite	Kaolinite	Montmorillonite	Kaolinite	Kaolinite	Kaolinite
Particle shape	Rod-like	Rod-like	Cuboid	Clump of spheres	Clump of spheres	Clump of spheres	Ellipsoids	Clump of spheres	Clump of spheres	Clump of spheres
Tangential force	Mohr-Coulomb-type tangential force	Mohr-Coulomb-type tangential force	Mohr-Coulomb-type tangential force	Mohr-Coulomb-type tangential force	/	Mohr-Coulomb-type tangential force	/	/	Hookean friction considered but as short-distance repulsion	Hookean friction considered but as short-distance repulsion
Friction parameters considered	$\varphi_s = 20°$ $k_s = 233\ N/m$	$\mu = 0.3$ $k_s = 285.6\ N/m$	$\varphi_s = 10°$ $k_s = 1500\ N/m$	$\varphi_s = 10°$ $k_s = 1500\ N/m$	$\mu = 0.3$ $k_s = 1.0\ N/m$	No friction coefficient included directly in simulations	/	/	k_s~14.3 N/m	k_s~14.3 N/m
Analyses performed	1D loading/ unloading	1D loading/ unloading	1D loading/ unloading	1D loading/ unloading	Suspensions, centrifuge tests	Sedimentation and 1D compression tests	Isotropic compression	Suspension	1D loading/ unloading	Triaxial compression and extension

Table 2. Parameters used with repulsive GB potential for Mono_1 sample calibration.

Parameter	Value
γ_{sb} $[-]$	0.37
ϵ $[J]$	2.36×10^{-24}
σ $[nm]$	230
ε_a $[-]$	850
ε_c $[-]$	250

Table 3. Parameters used with repulsive GB potential for Poly_1 sample calibration.

GB parameter	Type 1 – Type 1	Type 1 – Type 2	Type 1 – Type 3	Type 2 – Type 2	Type 2 – Type 3	Type 3 – Type 3
γ_{sb} $[-]$	0.35	0.32	0.32	0.305	0.305	0.39
ϵ $[J]$	1.4×10^{-25}	6.95×10^{-26}	6.95×10^{-26}	6.95×10^{-26}	6.95×10^{-26}	1.74×10^{-24}
σ $[nm]$	370	370	390	340	350	350
ε_{1a} $[-]$	1100	1100	1100	1050	1050	1050
ε_{1b} $[-]$	1100	1100	1100	1050	1050	1050
ε_{1c} $[-]$	600	600	600	470	470	300
ε_{2a} $[-]$	1100	1050	1050	1050	1050	1050
ε_{2b} $[-]$	1100	1050	1050	1050	1050	1050
ε_{2c} $[-]$	600	470	300	470	300	300

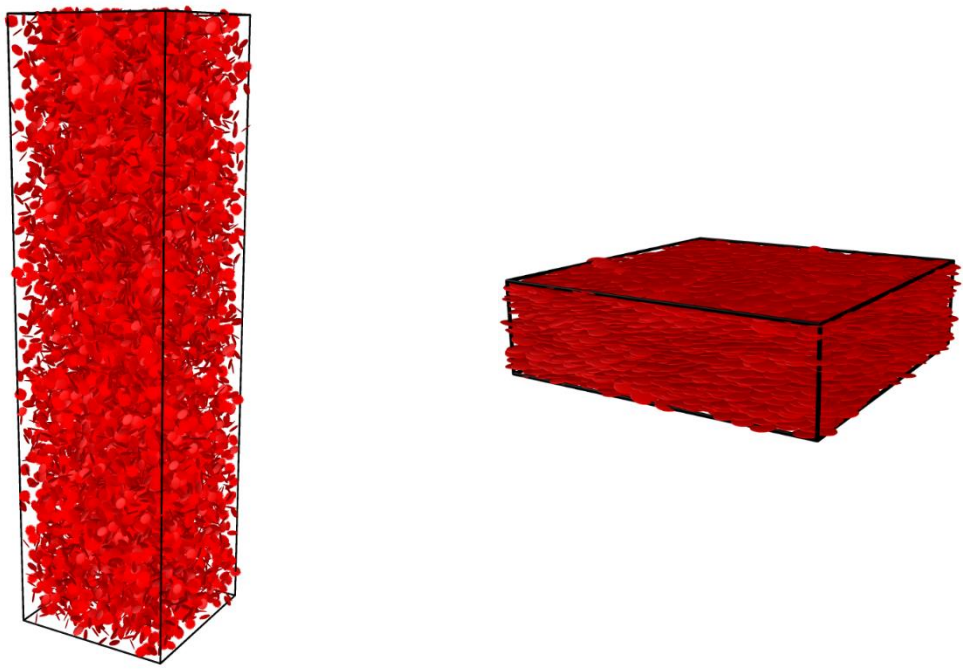

Figure 1. Snapshots of the particle arrangements within the Mono_1 specimen at the beginning (a) and at the end (b) of the one-dimensional compression test (Colour coded according to the particle type (Figure 1(a) and Figure 1(b) are not in scale).

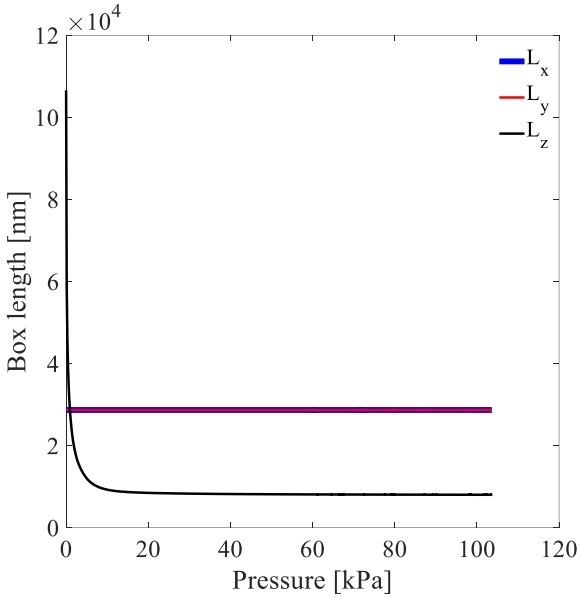

Figure 2. Deformation of the simulation box in x, y and z directions with pressure during a one-dimensional compression simulation for Mono_1 sample containing 10,000 particles and having an initial box aspect ratio of ~4.

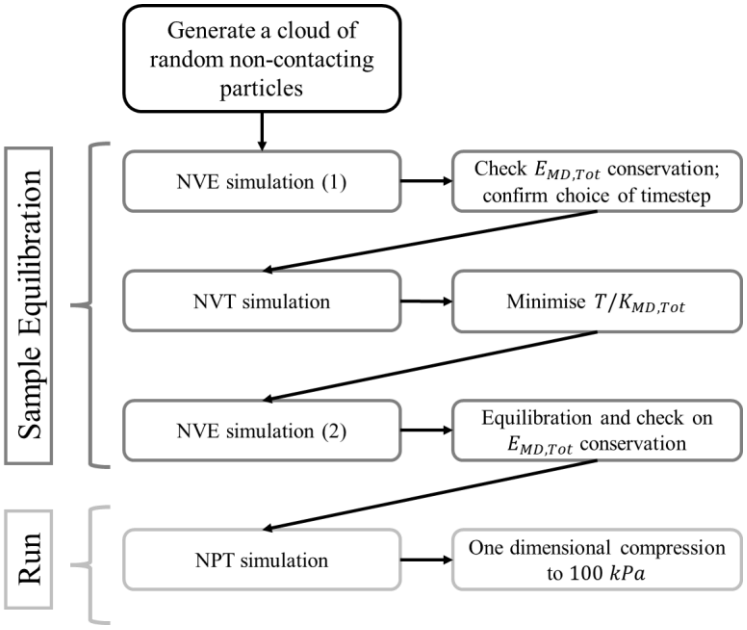

Figure 3. Workflow employed to perform molecular dynamics simulations of kaolinite considering alkaline pH conditions. T is the temperature of the system and $E_{MD,Tot}$ and $K_{MD,Tot}$ are the total energy and the kinetic energy of the system from the MD simulations, respectively (Bandera et al., 2021).

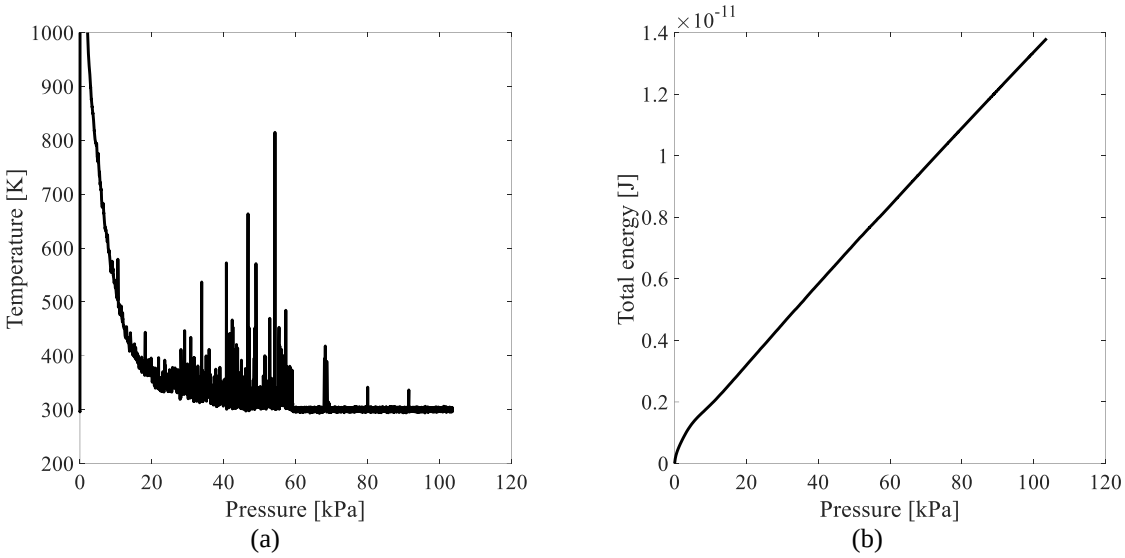

Figure 4. (a) Kinetic temperature and (b) total energy against applied vertical pressure profiles for the Mono_1 sample containing 10,000 particles.

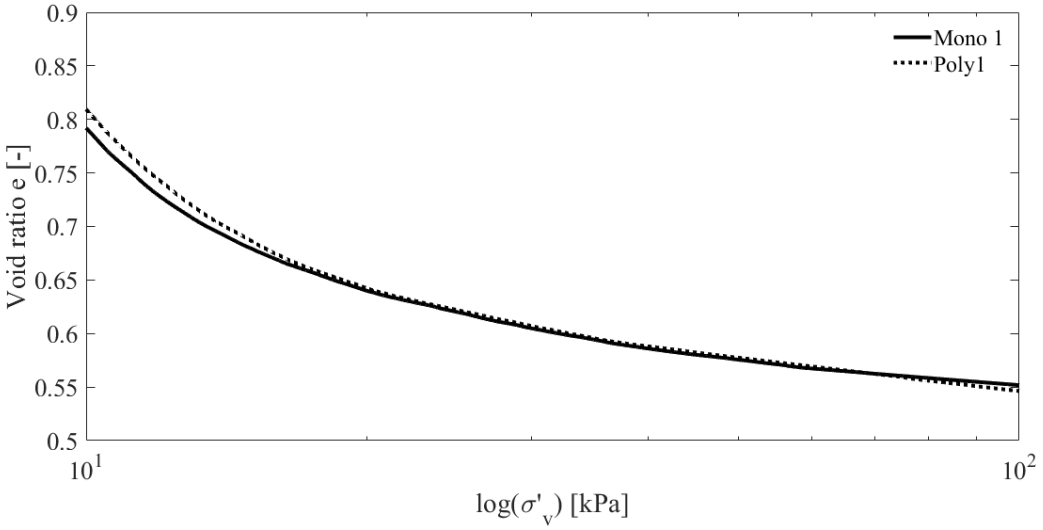

Figure 5. Void ratio-vertical effective stress σ_v' (e-log(σ_v')) profile for monodisperse (Mono_1) and slightly polydisperse (Poly_1) kaolinite samples saturated at alkaline pH and containing 10,000 particles.

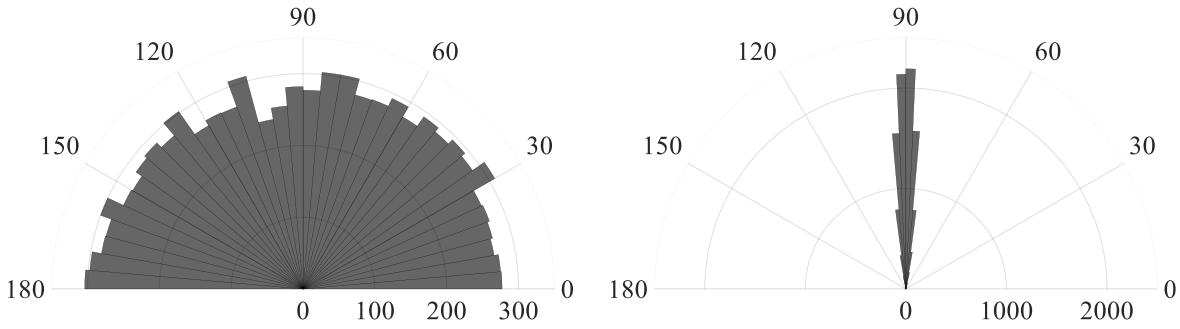

Figure 6. Rose diagrams showing the distribution of the particle orientations within the Mono_1 specimen; (a) at the beginning and (b) at the end of the one-dimensional compression.

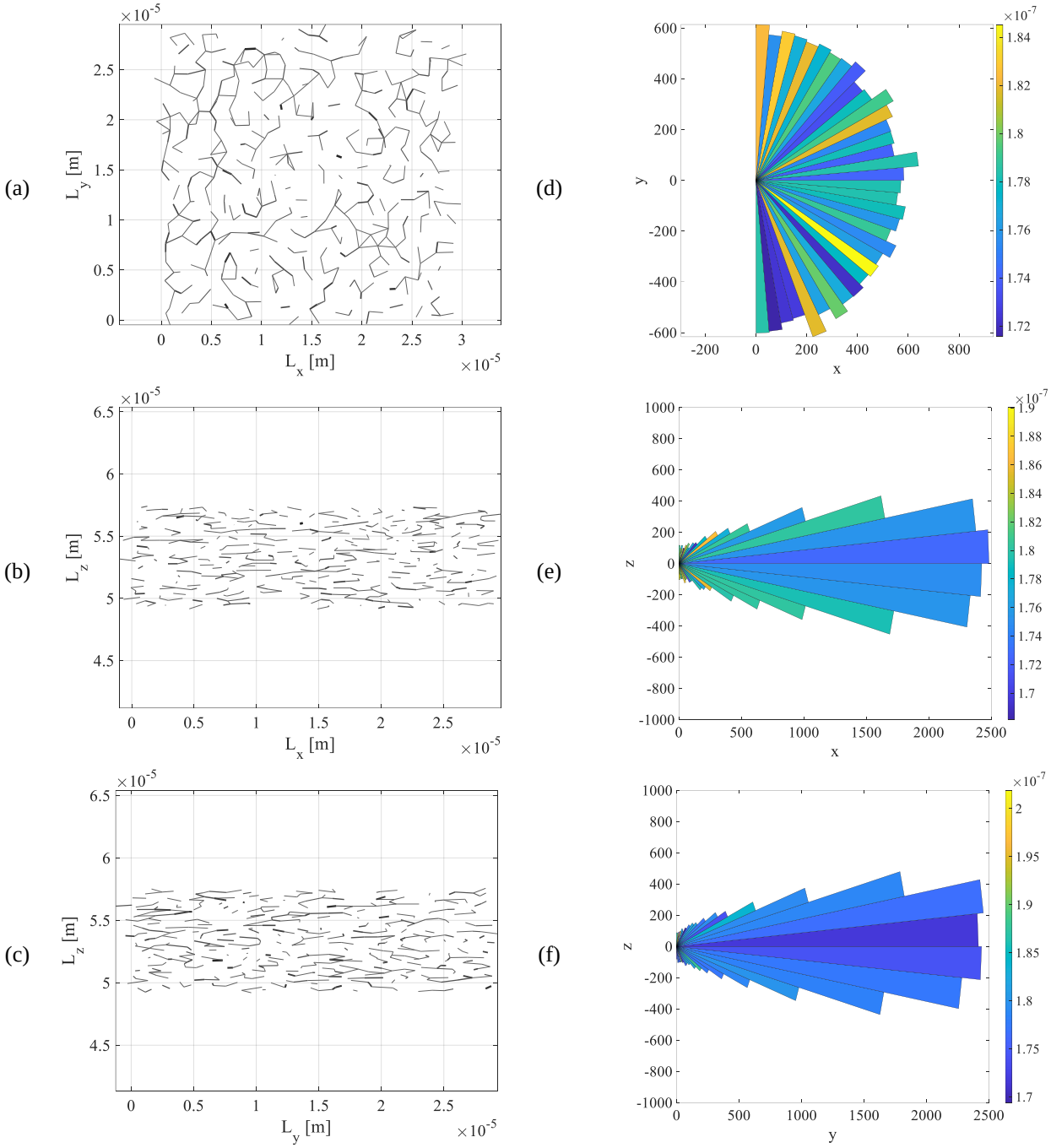

Figure 7. Force distribution within the one-dimensionally compressed Mono_1 sample considering (a) x-y, (b) x-z and (c) y-z planes and rose diagrams showing the orientation of contacts within the specimen in the (d) x-y, (e) x-z and (f) y-z planes. Results are coloured by average force, expressed in N; the stress level was 100 *kPa.*

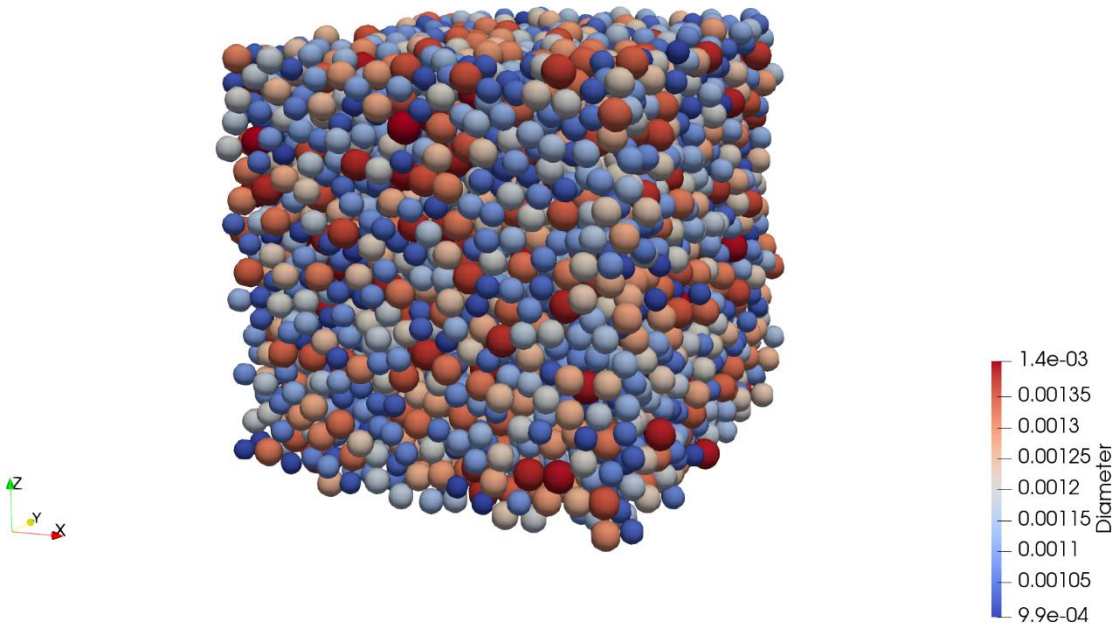

Figure 8. Snapshot of the DEM sample employed to perform one-dimensional compression tests.

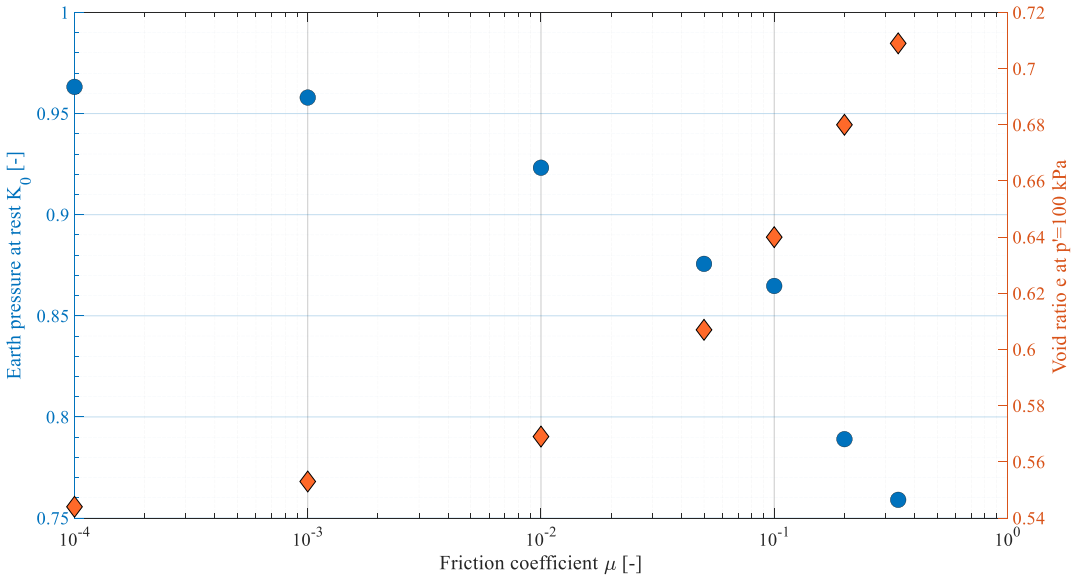

Figure 9. Summary of the values reached at the end of 1D compression at 100 *kPa by the coefficient of earth pressure at rest* K_0 *and for the void ratio* e_{100kPa} *obtained using DEM considering different friction coefficient values.*

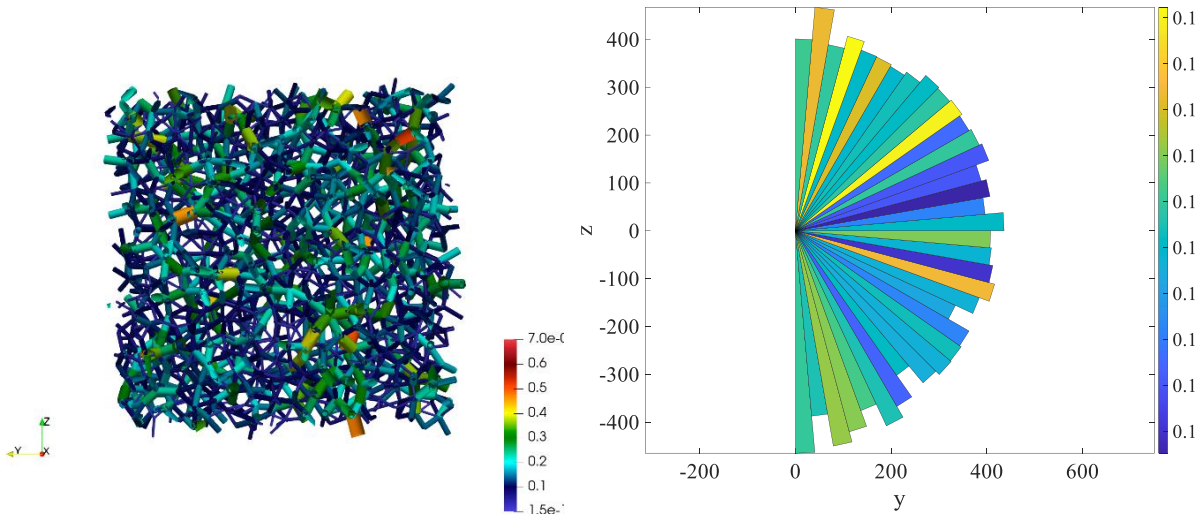

(a) (b)

Figure 10. (a) Two-dimensional projection of the contact network and (b) Rose diagram of the force distribution on the $y-z$ plane within the one-dimensionally compressed sample considering μ=1e-3. Results are coloured by average force, expressed in N.

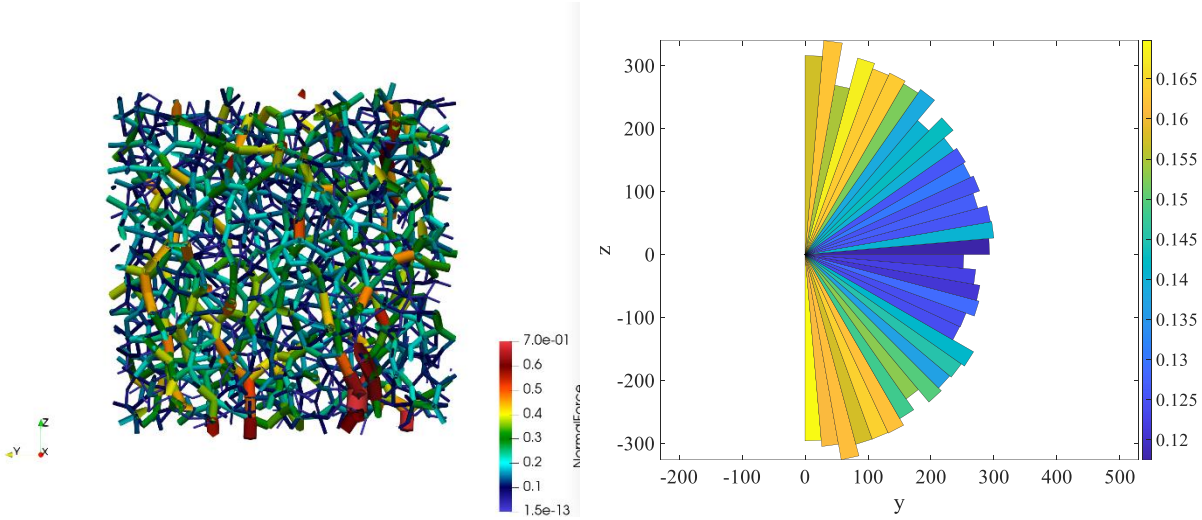

(a) (b)

Figure 11. (a) Two-dimensional projection of the contact network and (b) Rose diagram of the force distribution on the $y - z$ plane within the one-dimensionally compressed sample considering μ=0.34. Results are coloured by average force, expressed in N.